Stochastic protein interactions monitored by hundreds of single-molecule plasmonic biosensors

*Michael A. Beuwer, Menno W.J. Prins, and Peter Zijlstra**

Molecular Biosensing for Medical Diagnostics, Faculty of Applied Physics and Faculty of Biomedical Engineering, Eindhoven University of Technology, PO Box 513, 5600 MB, Eindhoven, The Netherlands

Institute for Complex Molecular Systems, Eindhoven University of Technology, PO Box 513, 5600 MB, Eindhoven, The Netherlands

ABSTRACT We present a plasmonic biosensor based on hundreds of individual gold nanorods with single-molecule sensitivity that are simultaneously monitored in real-time within a dark-field microscopy setup. The approach allows for the statistical analysis of single-molecule interactions without requiring any labelling of the analyte. We study an antibody-antigen interaction and find that the waiting-time distribution is concentration-dependent and obeys Poisson statistics. The ability to probe hundreds of nanoparticles simultaneously will provide a sensor with a dynamic range of 7 decades in concentration and will enable the study of heterogeneity in molecular interactions.

KEYWORDS nanoparticles, localized surface plasmon, biosensing, single-molecule

Single-molecule detection has distinct advantages over ensemble-averaged techniques because it yields statistical distributions of molecular properties instead of averages[1–4], and reveals rare and unsynchronized events[5–7]. Single-molecule microscopy largely relies on fluorescent labelling of biomolecules which precludes detection of analyte directly in biological fluids. This limitation is overcome by label-free biosensors[1,8–14] of which plasmonic nanoparticles are particularly attractive because they can be probed using far-field optics and their sensitivity relies solely on the refractive index of the analyte[15,16]. The electric field associated with a surface plasmon resonance decays rapidly into the surrounding medium and acts as a transducer that converts changes in the local refractive index into a frequency shift of the plasmon[17].

Planar plasmon sensors are commercially available and are widely used in biochemical laboratories to quantify average affinity parameters of molecules interacting with an extended sensor surface. Recently, single-molecule sensitivity has been achieved by using plasmonic structures with a strongly reduced surface area, i.e. individual gold nanorods[18,19]. Plasmon shifts were sensitively monitored on a single particle by either two-color photothermal microscopy[19] or single-particle spectroscopy[18]. However, these approaches require specialized equipment such as a pump-probe setup[19], or a supercontinuum laser combined with a sensitive spectrograph[18]. Secondly, neither approach provides sufficient statistics to determine distributions of molecular properties because a single particle exhibits only 5-10 binding sites. Here we overcome both limitations by monitoring hundreds of single-molecule plasmonic sensors in real-time using total-internal-reflection excitation in a standard microscope. We show that the waiting-time distribution of an antibody-antigen interaction obeys Poisson statistics and is concentration dependent. The parallelized detection promises a dynamic range of 7 decades in concentration, and the sensor is readily implemented in any laboratory.

Our sensor consists of individual gold nanorods (average size 10 nm x 40 nm) that were spincoated on a coverslip (see suppl. info for details). The sample was irradiated with a narrow-band light source in a prism-type total-internal reflection microscope (see Fig. 1a), and the scattered intensity of the particles was projected onto a CCD camera (Fig. 1b). In this back-ground free imaging geometry plasmon shifts induce changes in the scattering cross section at the illumination wavelength, causing variations in the detected scattered intensity (Fig. 1c).

The density of particles on the substrate was controlled by the concentration during spincoating to yield 150-250 particles in a 100 x 100 μm^2 field-of-view of the microscope. A fraction of the total field-of-view is displayed in Fig. 1b, where each diffraction limited spot represents a single nanorod. Each particle exhibits a different scattered intensity caused by (a) the inevitable dispersion in particle volume and aspect ratio[20] leading to a different scattering

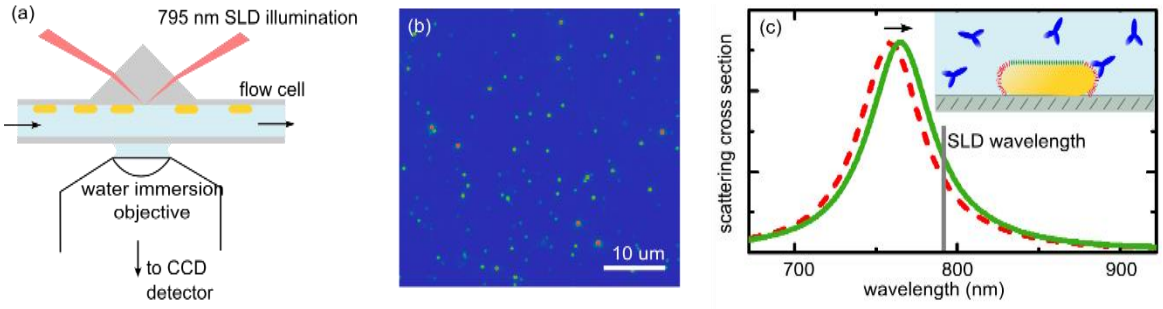

Figure 1 (a) Schematic of the optical setup (not to scale). SLD = superluminescent diode (Superlum, center wavelength 795 nm, bandwidth 14 nm, maximum power 35 mW), CCD = charge coupled device. (b) Typical CCD image of an area of 50 x 50 μm^2 on the sample surface. The field of view of the microscope is roughly 4 times the depicted area. The colour scale is linear and ranges from 0 (blue) to 16384 (red). (c) Cartoon of the detection principle. Gold nanorods are functionalized at their tips by receptors (depicted in red), whereas the sides are blocked with tetra-ethylene glycol (depicted in green). The binding of individual antibodies results in a red-shift of the plasmon resonance. The SLD's center wavelength is depicted by the vertical grey line.

cross-section at the irradiation wavelength, and (b) a different orientation of each particle in the partly polarized evanescent field. To ensure that we probe single nanorods we record white-light scattering spectra of all the particles (see suppl. info). We typically find that <10% of the particles are in clusters, which are discarded in the analysis.

The use of a superluminescent diode (SLD) as the light-source was crucial to achieve sufficient signal-to-noise ratio (S/N). The poor spatial coherence of light from an incandescent lamp provided insufficient intensity to image our small particles, whereas the high temporal coherence of laser illumination resulted in interference artefacts that induce signal fluctuations. SLD's are semiconductor high-gain devices that generate amplified spontaneous emission, and are widely used for optical coherence tomography because their reduced temporal coherence enables high-resolution imaging[21]. In our application the low temporal coherence of the SLD significantly reduced interference artefacts whereas the high spatial coherence ensured a high illumination intensity. This resulted in shot-noise limited signals (see suppl. info) for an integration time of 100 ms.

For nanorods, the plasmon shift is largest when the molecule binds at the tip due to the enhanced local field[22]. To promote binding at the tip we used a published protocol to achieve tip-specific functionalization with thiolated biotin-receptors[23] (see suppl. info). The remainder of the particle surface was blocked by thiolated tetra-ethylene glycol (PEG4) to suppress non-specific interactions. In a typical single-molecule experiment we flush antibiotin (molecular weight 150 kDa) into the flowcell using a syringe pump and use the CCD camera to record the time-dependent scattered signal (determined by a two-dimensional Gaussian fit of each spot in each frame). Plasmon shifts caused by biomolecular binding are then observed as step-wise changes in the scattered intensity.

Two examples of the resulting time-traces are shown in Fig. 2a, where we observe step-wise changes of the scattered intensity due to stochastic binding of individual antibodies. The magnitude of the steps varies from 1 to 5%, which is in good agreement with previous numerical calculations[19]. The distribution of step-sizes can be attributed to the different position and

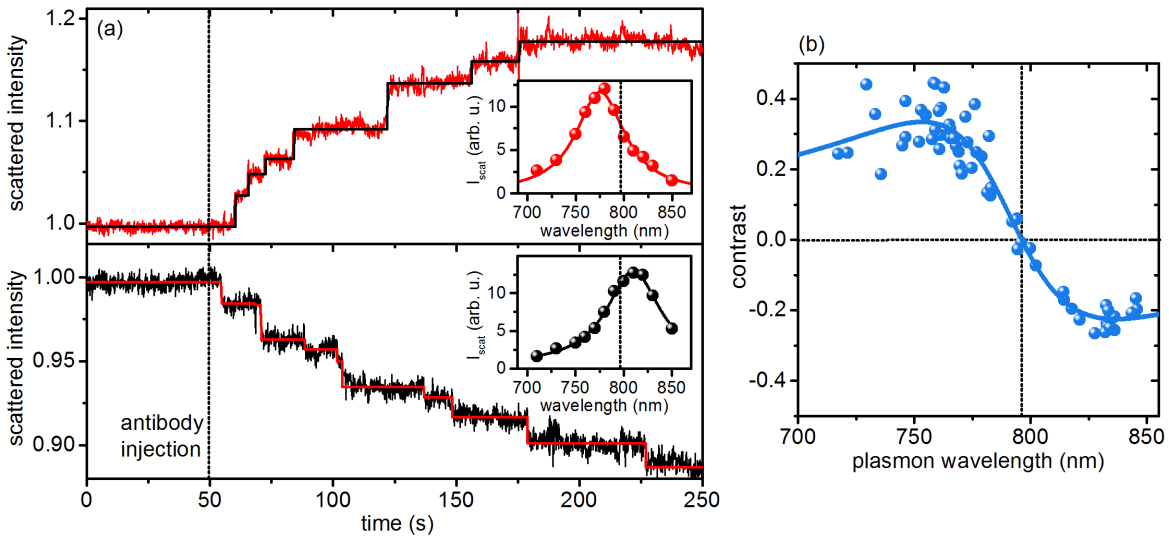

Figure 2. (a) Time-trace of the normalized scattered intensity of two individual nanorods in the same field-of-view but with two different longitudinal plasmon wavelengths. Solid lines are fits to the datapoints using a stepfinding algorithm (see text for details). Stepwise changes in the signal indicate stochastic binding of single antibodies (antibody concentration 10 nM). The sign of the stepwise changes (positive at the top, negative at the bottom) depends on the plasmon wavelength relative to the wavelength of the irradiation source. The measured white-light scattering spectrum of the respective particle is shown in the insets (the dotted line represents the center wavelength of the SLD). (b) Correlation between the measured plasmon wavelength of several individual nanorods and the observed contrast ($I_{final} - I_{start}$, where I_{final} was measured at t=700 seconds after antibody injection). The vertical dashed line indicates the SLD's center wavelength. The solid line represents a fit to the data points obtained from the difference spectrum in the dipole approximation.

orientation of each antibody in the rapidly decaying near-field at the particle's tips. The sign of the signal caused by antibody binding depends on the plasmon wavelength relative to the SLD wavelength. For particles with a plasmon wavelength shorter than the SLD wavelength the red-shift of the plasmon causes an increase in the scattered signal (top curve in Fig. 2a), whereas particles with a plasmon wavelength longer than the SLD wavelength exhibit the opposite behavior (bottom curve in Fig. 2a). In Fig. 2b we show the correlation between plasmon wavelength and the sign of the signal, which follows the expected behavior.

To ensure that the binding events we observe are due to specific interactions (i.e. interactions of the antibody with biotin on the particle surface) we also performed control experiments on particles coated with PEG4 only (see suppl. info). In the control experiments we did not observe a persistent signal and we thus conclude that the signals in Fig. 2a are due to specific interactions.

To analyze the waiting-time distributions (i.e. the time between binding events), we fit the time-traces of all particles using a step-finding algorithm[24]. An example of a timetrace including a step-fit is shown in Fig. 3a. The full distribution of waiting times is obtained by analyzing the timetraces of all particles in the field-of-view. A fraction of the particles does not exhibit step-wise changes of the signal because the plasmon wavelength is close to the SLD wavelength. For that reason we excluded particles with a plasmon resonance between 775 nm and 815 nm. We also excluded steps with a S/N < 2 (defined as the ratio between step-size and standard-deviation of the signal before antibody injection) which we attribute to drift of the background or antibodies binding to the glass surface close to the particles.

The extracted distribution of t_{on} is shown in Fig. 3b. We only included the first 5 binding events in the analysis to exclude steric effects due to crowding and saturation on the particle

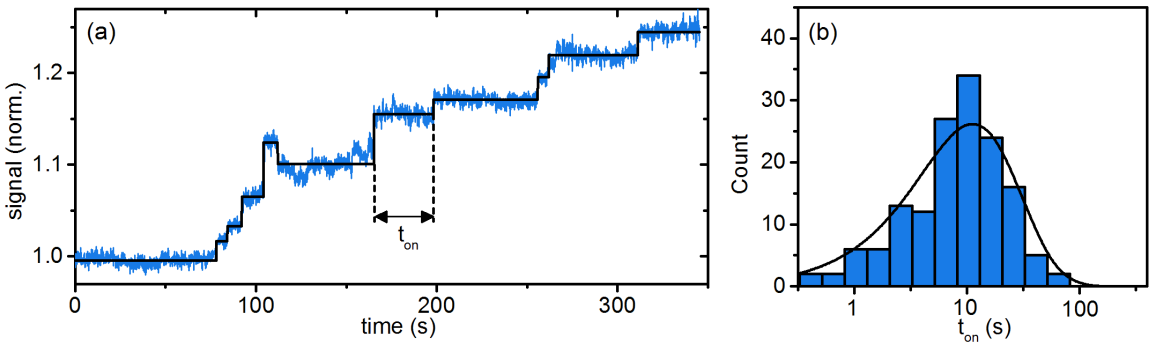

Figure 3 (a) Time-trace of the scattered intensity of a single nanorod (10 nM antibody injected at t=60 s). The solid line shows a fit with a step-finding algorithm, from which we obtained the waiting-time between binding events, t_{on}. (b) The distribution of t_{on} for 10 nM antibody concentration, obtained by analysis of many single-molecule biosensors in the field-of-view of the microscope.

surface. In case of a single rate-limiting step, the probability that a binding event occurs within a time t_{on} is Poisson distributed:

$$P(t_{on}) = \frac{t_{on}}{\tau} e^{-\frac{t_{on}}{\tau}}, \qquad (1)$$

where τ is the mean waiting-time. Both the mean and the standard deviation of the distribution increase linearly with time. For a concentration c = 10 nM we find $\tau = 12 \pm 1$ s by fitting the distribution using Eq. (1). The association rate constant for binding to a single nanoparticle (NP) is then given by

$$k_{on}^{NP} = \frac{1}{\tau\, c} = 8.3 \times 10^6\, M^{-1} s^{-1}. \qquad (2)$$

This relates to a molecular association rate constant $k_{on} = k_{on}^{NP}/N_{sites}$ where N_{sites} represents the number of binding sites per particle. By counting the number of binding events in the timetraces we estimate $N_{sites} = 10$ on average, which leads to $k_{on} = 8.3 \times 10^5$ $M^{-1}s^{-1}$.

Although no literature reports were found for our specific antibody-antigen system, this k_{on} is in good agreement with literature values for other antibody-antigen pairs[25–28] and with our own ensemble-averaged results (see suppl. info).

We investigated the concentration dependence of τ by employing a range of antibody concentrations, see Fig. 4. For each concentration we see a distribution of waiting-times that obeys Poisson statistics, with a mean binding rate $1/\tau$ that depends on the concentration. In Fig. 4b we show the concentration dependence of the mean binding rate, in agreement with a first-order powerlaw.

We now analyze the potential dynamic range of the sensor by distinguishing a low- and high concentration regime. Low analyte concentrations limit the statistics because the binding rate is low. The average number of binding events N_{avg} that is observed in a certain time window t is given by (assuming a single rate-limiting step)

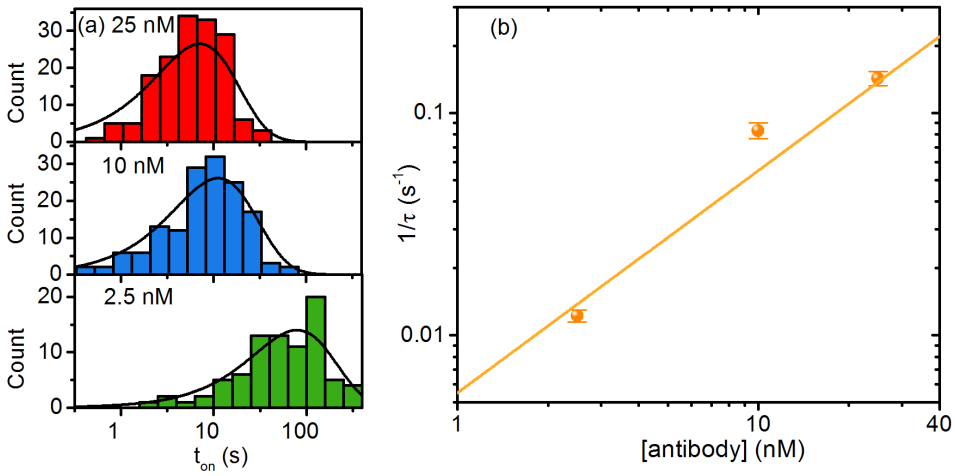

Figure 4 (a) Waiting-time distributions for different antibody concentrations. The solid lines are Poissonian fits using Eq. (1). (b) Dependence of the mean binding rate on the antibody concentration. The solid line is a first-order powerlaw. The error bars are fitting errors obtained from the Poisson fits in (a).

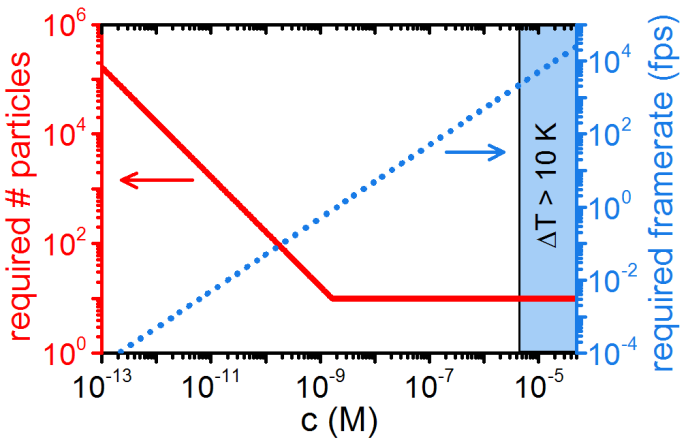

Figure 5 Projected dynamic range of the presented single-molecule biosensor. The left axis displays the number of particles required to observe 100 events in 10 minutes. The right axis displays the frame-rate required to resolve single-molecule binding events. The maximum accessible concentration of ≈ 5 µM (indicated by the vertical line on the right) is limited by nanoparticle heating caused by the increased incident intensity required to achieve sufficient S/N.

$$N_{avg} = \frac{1}{\tau} N_{pcle} t = k_{on}^{NP} c \, N_{pcle} t, \tag{3}$$

with N_{pcle} the number of particles in a field-of-view. If we require $N_{avg} = 100$ to reliably establish a distribution function within 10 minutes, we find that for $c > 3$ nM we only require 10 particles because all 10 binding sites on the particle will be occupied at least once. For $c < 3$ nM the required number of particles scales inversely with the analyte concentration, see the left axis in Fig. 5. The minimum accessible concentration is then determined by N_{pcle}. The 2D Gaussian fitting algorithm currently requires a region-of-interest of 10x10 pixels to obtain an accurate fit for our magnification of 60x. High-end scientific cameras having a resolution of >5 megapixels, we estimate that $N_{pcle} \approx 50.000$ is achievable under optimum conditions. The lowest accessible

concentration is then $c \approx 0.5$ pM. Note that increasing the measurement time is an equivalent approach but might require active stabilization of the incident intensity and the thermal drift of the setup[29], whereas N_{pcle} is easily tuned by employing samples with controlled particle densities.

Higher analyte concentrations exhibit an increased rate of binding, for which a higher framerate (i.e. a shorter integration time) is required to resolve all single-molecule binding events. Based on the Poisson distributed waiting times we set the required framerate to $50/\tau$ to ensure that the short times in the distribution are also resolved, see the blue dotted line in Fig. 5. By increasing the incident intensity from 64 W/cm^2 to 1 kW/cm^2 we reduced the integration time to 6 ms with only a modest reduction in S/N. However, our camera did not allow us to record continuous time-series for longer than a few seconds using these parameters. The maximum framerate that can be achieved is fundamentally limited by the photothermal heating of the nanoparticles. For studies on biological samples the maximum permissible temperature rise is of the order of 10 K, which we estimate is reached for an incident intensity of 10 kW/m^2 (see suppl. info). This implies that a framerate of 20.000 fps ($t_{int} = 500\ \mu s$) is achievable without inducing thermal damage to the analyte. Such high frame-rates give access to low-affinity interactions or to analyte concentrations as high as $\approx 5\ \mu M$ (see Fig. 5).

In the above analysis we assumed the limiting case that each binding site can only be occupied once during a time-window of 600 s. This situation occurs for antibody-antigen interactions with a high affinity and therefore a low dissociation rate. For low-affinity interactions, dissociation can occur during the measurement time so each binding site may be occupied multiple times. The number of particles required to establish a certain number of detection events will thus be lower.

Probes for biosensing with single-molecule resolution (e.g. a metal nanoparticle, a dielectric resonator, a solid-state nanopore) typically exhibit a limited dynamic range due to the low number of binding sites per probe, prohibiting the accumulation of sufficient statistics at low analyte concentrations. This limitation is overcome here by the parallelized probing of many sensors, giving an extraordinary projected dynamic range of 7 decades in concentration. The ability to extract distributions of molecular interaction parameters enables the investigation of heterogeneity in a population of unlabeled molecules. The simple and cheap optical layout will allow the sensor to be implemented in any laboratory with a microscope.

ASSOCIATED CONTENT

Supporting Information. Details on sample preparation, nanoparticle functionalization, white-light spectroscopy, signal-to-noise ratio, specificity of the interactions, ensemble-averaged results, and estimated particle temperature. This material is available free of charge via the Internet at http://pubs.acs.org.

AUTHOR INFORMATION

Corresponding Author

* p.zijlstra@tue.nl

Author Contributions

M.P. and P.Z. conceived the experiments, M.B. and P.Z. performed the experiments, M.B. and P.Z. analyzed the data, all authors co-wrote the paper. All authors have given approval to the final version of the manuscript.

ACKNOWLEDGMENT

P.Z. acknowledges financial support by the Netherlands Organisation for Scientific Research (NWO). M.P. and P.Z. acknowledge financial support from the Netherlands 3TU Federation.

REFERENCES

(1) Wei, R.; Gatterdam, V.; Wieneke, R.; Tampé, R.; Rant, U. *Nat. Nanotechnol.* **2012**, *7*, 257–263.

(2) Verbrugge, S.; Lansky, Z.; Peterman, E. J. G. *Proc. Natl. Acad. Sci. U. S. A.* **2009**, *106*, 17741–17746.

(3) Van Oijen, A. M. *Curr. Opin. Biotechnol.* **2011**, *22*, 75–80.

(4) Jain, A.; Liu, R.; Xiang, Y. K.; Ha, T. *Nat. Protoc.* **2012**, *7*, 445–452.

(5) Van Oijen, A. M.; Blainey, P. C.; Crampton, D. J.; Richardson, C. C.; Ellenberger, T.; Xie, X. S. *Science* **2003**, *301*, 1235–1238.

(6) Kim, E.; Lee, S.; Jeon, A.; Choi, J. M.; Lee, H.-S.; Hohng, S.; Kim, H.-S. *Nat. Chem. Biol.* **2013**, *9*, 313–8.

(7) Janssen, K. P. F.; De Cremer, G.; Neely, R. K.; Kubarev, A. V; Van Loon, J.; Martens, J. A.; De Vos, D. E.; Roeffaers, M. B. J.; Hofkens, J. *Chem. Soc. Rev.* **2014**, *43*, 990–1006.

(8) Sorgenfrei, S.; Chiu, C.; Gonzalez, R. L.; Yu, Y.-J.; Kim, P.; Nuckolls, C.; Shepard, K. L. *Nat. Nanotechnol.* **2011**, *6*, 126–132.

(9) Cognet, L.; Tsyboulski, D. A.; Rocha, J.-D. R.; Doyle, C. D.; Tour, J. M.; Weisman, R. B. *Science* **2007**, *316*, 1465–1468.

(10) Ahn, J. H.; Kim, J. H.; Reuel, N. F.; Barone, P. W.; Boghossian, A. A.; Zhang, J.; Yoon, H.; Chang, A. C.; Hilmer, A. J.; Strano, M. S. *Nano Lett.* **2011**, *11*, 2743–2752.

(11) Cui, Y.; Wei, Q.; Park, H.; Lieber, C. M. *Science* **2001**, *293*, 1289–1292.

(12) Dekker, C. *Nat. Nanotech.* **2007**, *2*, 209–215.

(13) Vollmer, F.; Arnold, S. *Nat. Methods* **2008**, *5*, 591–596.

(14) Dantham, V. R.; Holler, S.; Barbre, C.; Keng, D.; Kolchenko, V.; Arnold, S. *Nano Lett.* **2013**, *13*, 3347–3351.

(15) Anker, J. N.; Hall, W. P.; Lyandres, O.; Shah, N. C.; Zhao, J.; Van Duyne, R. P. *Nat. Mater.* **2008**, *7*, 442–453.

(16) Brolo, A. *Nat. Photonics* **2012**, *6*, 709–713.

(17) Mayer, K. M.; Hafner, J. H. *Chem. Rev.* **2011**, *111*, 3828–3857.

(18) Ament, I.; Prasad, J.; Henkel, A.; Schmachtel, S.; Sönnichsen, C. *Nano Lett.* **2012**, *12*, 1092–1095.

(19) Zijlstra, P.; Paulo, P. M. R.; Orrit, M. *Nat. Nanotechnol.* **2012**, *7*, 379–382.

(20) Eustis, S.; El-Sayed, M. A. *J. Appl. Phys.* **2006**, *100*, 044324.

(21) Ko, T. H.; Adler, D. C.; Fujimoto, J. G.; Mamedov, D.; Prokhorov, V.; Shidlovski, V.; Yakubovich, S. *Opt. Express* **2004**, *12*, 2112–2119.

(22) Liu, M.; Guyot-Sionnest, P.; Lee, T. W.; Gray, S. K. *Phys. Rev. B* **2007**, *76*, 235428.

(23) Zijlstra, P.; Paulo, P. M. R.; Yu, K.; Xu, Q. H.; Orrit, M. *Angew. Chemie - Int. Ed.* **2012**, *51*, 8352–8355.

(24) Kerssemakers, J. W. J.; Munteanu, E. L.; Laan, L.; Noetzel, T. L.; Janson, M. E.; Dogterom, M. *Nature* **2006**, *442*, 709–712.

(25) Rispens, T.; Te Velthuis, H.; Hemker, P.; Speijer, H.; Hermens, W.; Aarden, L. *J. Immunol. Methods* **2011**, *365*, 50–57.

(26) Im, H.; Sutherland, J. N.; Maynard, J. A.; Oh, S. H. *Anal. Chem.* **2012**, *84*, 1941–1947.

(27) Karlsson, R.; Michaelsson, A.; Mattsson, L. *J. Immunol. Methods* **1991**, *145*, 229–240.

(28) Gabdoulline, R. R.; Wade, R. C. *Curr. Opin. Struct. Biol.* **2002**, *12*, 204–213.

(29) Elenko, M. P.; Szostak, J. W.; Van Oijen, A. M. *Rev. Sci. Instrum.* **2010**, *81*, 083705.

TOC Graphic